Water Research 171 (2020) 115479

Contents lists available at ScienceDirect

Water Research

journal homepage: www.elsevier.com/locate/watres

Cyclical patterns and (im)mobilization mechanisms of phosphorus in sediments from a small creek estuary: Evidence from *in situ* monthly sampling and indoor experiments

Feng Pan [a], Zhanrong Guo [a, *], Yu Cai [a], Yuyao Fu [a], Jinye Wu [a], Bo Wang [a], Huatai Liu [b], Aiguo Gao [a, c]

[a] College of Ocean and Earth Sciences, Xiamen University, Xiamen, 361102, PR China
[b] College of the Environment and Ecology, Xiamen University, Xiamen, 361102, PR China
[c] State Key Laboratory of Marine Environmental Science, Xiamen University, Xiamen, 361102, PR China

ARTICLE INFO

Article history:
Received 19 June 2019
Received in revised form
24 December 2019
Accepted 6 January 2020
Available online 7 January 2020

Keywords:
Diffusive gradients in thin films
High-resolution peeper
High-resolution spatiotemporal sampling
Tidal simulation experiment
Phosphorus mobility
Small creek estuary

ABSTRACT

Internal phosphorus (P) mobility is crucially important to overlying water ecosystems, while its spatiotemporal variations and mechanisms remain to be studied, especially in dynamic estuarine sediments. In this study, *in situ* monthly field sampling and indoor experiments were combined to measure the soluble reactive P (SRP), soluble Fe and diffusive gradients in thin films (DGT)-labile P/S in the overlying water, sediment and porewater in the Jiuxi River Estuary by employing high-resolution dialysis (HR-Peeper), the DGT technique and a MicroRhizon sampler. The consistent tendency between DGT-labile S and P in most seasons indicates that P mobilization was dominated by intense dissimilatory sulfate reduction (DSR), causing high SRP concentrations and active exchange with the overlying water. The circannual cyclical pattern of P is summarized, where in addition to temperature, monthly changes in runoff and tidal range are crucial external factors to control long-term P cycling via changed redox environments and terrigenous materials inputs. The mobile P, Fe and S present higher values during flood tides and lower values during ebb tides in tidal simulation experiments, demonstrating that the short-term cycling of P, Fe and S in intertidal surface sediments is highly redox-sensitive and controlled by tidal processes. The results also reveal that DSR greatly facilitates P mobility and release, while sediment oxidation and the induced enhancement in DIR and Fe cycling can effectively control P immobilization.

1. Introduction

Phosphorus (P) is commonly deemed the ultimate limiting nutrient at geologic timescales, with the bioavailable P effectively controlling oceanic primary productivity and thus global carbon cycling (Conley et al., 2009; Tyrrell, 1999). Marine sediments and porewater are crucial biogeochemical reactors of mobile (diagenetically reactive) P, which can act as sources or sinks of P to the overlying water (Markovic et al., 2019; Pan et al., 2019c). The degree to which bioavailable P is trapped in the sediment, as opposed to being exported to the overlying water, is generally redox dependent (Xiong et al., 2019). Overlying water hypoxia and an anoxic depositional context facilitate a decrease in the sequestration capacity of the sediment for P and accelerate anaerobic P mineralization and liberation, both of which can promote the release of soluble reactive P (SRP) to the overlying water and positive productivity feedback to deteriorate the water quality (Conley et al., 2002; Middelburg and Levin, 2009). In addition, a high overlying water SRP content can also be retained in the surface oxic sediment, which acts as a potential labile P pool for internal P loading under favorable biogeochemical conditions (Pan et al., 2019c).

Sediment internal P mobility has a tight connection with the biogeochemical cycling of iron (Fe) and sulfur (S) (Rozan et al., 2002). Dissimilatory sulfate reduction (DSR) and dissimilatory Fe(III) reduction (DIR) are two major pathways for marine organic matter (OM) diagenetic mineralization, accompanied by anaerobic organic P mineralization, which are crucial processes for diagenetic P mobilization (Markovic et al., 2019; Rozan et al., 2002). SRP has a strong affinity to poorly crystalline and amorphous Fe(III) (hydr)

* Corresponding author.
E-mail address: gzr@xmu.edu.cn (Z. Guo).

https://doi.org/10.1016/j.watres.2020.115479
0043-1354/

oxide surfaces, leading to significant scavenging of the SRP from solution (Slomp et al., 1996). Under anoxic conditions, Fe(III) (hydr) oxides are partially dissolved through DIR, releasing absorbed P into the ambient porewater (Lovley and Phillips, 1988). In addition, DSR and sulfide have been found to facilitate P remobilization by chemical Fe(III) reduction to coprecipitate FeS and FeS_2, which have minimal affinities for P sequestration (Ingall and Jahnke, 1997; Lehtoranta et al., 2009). Considering their close relationship, detailed insight into the relevant processes of Fe and S redox cycling is of particular significance to understand P mobility in marine sediments.

As the transition of ocean to land, an estuary is especially sensitive to increasing (anthropogenic) P input, which can fuel the development of hypoxia and algal blooms (Kraal et al., 2015). The sequestration and release processes of P in estuarine sediments are highly significant for the global oceanic P cycle, as the sediment represents a vital P source for the open ocean (Paytan and McLaughlin, 2007). In light of the mounting global climate changes, such as sea level rise and runoff changes, which can result in persistent or temporary aquatic hypoxia, the benthic P cycling in estuaries may be notably converted in response to hypoxia and eutrophication (Diaz and Rosenberg, 2008). Therefore, clarifying the redox-dependent P (im)mobilization processes and release mechanisms in eutrophicated estuaries is essential. In addition, the depositional and hydrodynamic conditions in an estuary are so dynamic that waves, tides, river runoff, bioturbation and deposition rates are highly variable in both the long term (monthly/seasonal) and short term (tidal/diurnal). Diagenetic P cycling in this environment is complicated and dynamic and may exhibit strong spatial and temporal heterogeneity (Pan et al., 2019c; Rozan et al., 2002). Nevertheless, high-frequency field studies of P geochemistry and related processes have been insufficient; most study are seasonal (e.g., summer and winter) (Markovic et al., 2019; Pan et al., 2019c; Rozan et al., 2002), and the cyclical pattern of P is not complicated because many environmental factors have not been considered. Further monthly field surveys and hourly indoor incubation are imperative to better understand the spatiotemporal variations in key chemicals and to summarize the cyclical pattern and (im)mobilization mechanisms of P, which are crucial to predict its geochemical fate and control its pollution.

Previous studies on internal P cycling have paid more attention to intermediate and large river estuaries, such as the Jiulong River Estuary, Yangtze River Estuary and the mouth of the Mississippi River (Cao et al., 2017; Pan et al., 2017; Roy et al., 2017), while usually ignoring fairly small creeks. However, a small creek may be highly polluted and eutrophic (black malodorous water) due to industrial and agricultural activities, which lack government oversight, and such a creek may have a low self-purification capacity (Yin et al., 2019). Clarifying the cyclical pattern and (im) mobilization mechanisms of P in this environment can provide a new insight into estuarine P pollution treatment especially against the background of climate changes (sea level rise and runoff changes) and anthropogenic activities. In this study, the monthly distribution of mobile P, Fe and S in the sediments and porewater of the Jiuxi River Estuary were determined using *in situ* high-resolution dialysis (HR-Peeper) and diffusive gradients in thin films (DGT) samplers, based on which the mobility and pollution of P in estuarine sediments were assessed, and a circannual cyclical pattern of P was summarized. To explore the effects of tides on the short-term changes in Fe and S cycling and related P (im)mobilization, a novel indoor tidal simulation experiment was further conducted to study the hourly changes in P, Fe and S during tidal oscillation using a MicroRhizon sampler and a DGT probe.

2. Materials and methods

2.1. Description of the study site

The study site (24°35′38″N, 118°16′42″E) is located in the estuary of the Jiuxi River (Fig. S1), which is a fairly small creek (approximately 20 km long) with a narrow watercourse (dozens of meters wide) and a long estuary because of macrotides with a mean tidal range of 4.1 m. In addition to the strong tides, the water level and hydrological conditions in the estuary are seasonally influenced by runoff. This region has a subtropical oceanic monsoon climate with a mean annual air temperature of 21.0 °C and a mean annual rainfall of 1350 mm, of which ~70% occurs between April and September (Jin et al., 2013). In contrast to large rivers, the runoff of the Jiuxi River is principally influenced by occasional heavy rainfall. As shown in Table S1, the dissolved oxygen (DO) concentrations indicate some hypoxia, especially in summer and autumn, and the overlying water is basically alkalescent. The SRP concentrations in the adjacent Xiamen Bay are up to two times higher than those allowed by Chinese sea water quality standards (Liao et al., 2013) and are considered as the main reason for frequent eutrophication events and blooms (Yang et al., 2012).

2.2. Preparation of the DGT and HR-Peeper probes

The HR-Peeper sampler contained 36 equally spaced 400 μL chambers fully loaded with deionized water with a 5 mm vertical resolution, and the chambers were covered by a cellulose nitrate membrane (0.45 μm pore size, Whatman). The principle of the HR-Peeper is based on diffusion equilibrium, allowing solutes to diffuse across the membrane and achieve equilibrium after some time (Teasdale et al., 1995). The DGT technique is a dynamical technique based on Fick's first law of diffusion and has the potential to conduct *in situ* measurements of the labile species in sediments with a high resolution (Davison and Zhang, 1994). The DGT-measured P/S comes from the porewater SRP/dissolved sulfide and the further release of solid easily exchangeable or mobile P/S fractions to resupply the porewater, which is referred to as DGT-labile P/S (Zhang et al., 1995). Therefore, the DGT uptake process involves dynamic solid-solution interactions of chemicals, which are affected by their solid lability.

All HR-Peeper and ZrO–AgI DGT probes, provided by Easy Sensor Ltd. (www.easysensor.net), were prepared according to Xu et al. (2012) and Ding et al. (2012). The HR-Peeper and ZrO–AgI DGT devices were stored in deionized water in the dark and deoxygenated with nitrogen for one day prior to deployment.

2.3. Field methods

During the low-tide period in each month from May 2018 to April 2019, one HR-Peeper probe was first inserted into the sediment with four chambers (2 cm) above the sediment-overlying water interface (SWI) and deployed for one day. A ZrO–AgI DGT probe was then inserted very close to the HR-Peeper, and the probes were both deployed for one more day. The probes were retrieved from the sediment simultaneously and carefully cleaned. After that, porewater samples were rapidly collected using a pipette, a portion of which was acidified with HNO_3 for the analysis of soluble Fe. The DGT probes were kept moist and out of the sun prior to analysis. A handheld YSI Professional Plus device was used to measure the overlying water properties during sampling in each month starting in July.

After retrieval of the HR-Peeper and DGT probes in each month, sediment cores or surface sediments were immediately collected using hollow PVC tubes. In July, October, January and April,

sediment cores were collected and sectioned at 1 cm intervals (uppermost 5 cm) or 2 cm intervals (6–15 cm). In the remaining months, only the surface 5 cm of sediments were collected. These samples were sealed in polyethylene bags that had been deoxygenated with nitrogen beforehand and quickly transported to the laboratory for further analysis.

2.4. Indoor experiments

Two sediment cores and overlying water were collected using a homemade disassembled poly(methyl methacrylate) (PMMA) tube and buckets at the sampling site and transported to the laboratory. In the control group, ten MicroRhizon samplers (Rhizon CSS, the Netherlands) were inserted into the undisturbed sediment (Fig. S2). To simulate the diurnal tide in the intertidal zone, a peristaltic pump drew overlying water from the bucket to the incubator at a rate of a 2 m head in 6 h. Then, the overlying water was drawn back to the bucket at the same rate, followed by exposure in the next 12 h. In the experimental group, the sediment was mixed and homogenized in one day for intensive oxidization. Then, MicroRhizon samplers were inserted, and the tide cycle was simulated as for the control group, both of which underwent another 3 tide cycles prior to sampling.

One ZrO–AgI DGT probe was deployed in the sediments of the control group and one in those of the experimental group. Then, the simulated flood tide began. Approximately 0.5 mL porewater was extracted from the inserted MicroRhizon sampler by a vacuum tube every 3 h. When the simulated ebb tide began, the DGT probe was retrieved during the flood tide, and another DGT probe was deployed during the ebb tide. Throughout the experiment, the porewater was sampled eight times, and two DGT probes were deployed for each group.

2.5. Chemical analyses

For DGT-labile S analysis, the binding gels of the ZrO–AgI DGT probes were immediately cut along the open window and scanned using a scanner (Canon 5600F) with a resolution of 600 dpi, which corresponds to a pixel size of 0.042 mm × 0.042 mm. The scanned images were analyzed with ImageJ 1.46 to convert the images into grayscale intensities (Widerlund and Davison, 2007). Afterwards, the gels were cut into strips at 5 mm vertical intervals using ceramic knives. The DGT-labile P was extracted by adding 1.0 M NaOH solution to the strips (Ding et al., 2012). The concentrations of SRP and soluble Fe in the porewater and overlying water sampled by the HR-Peeper and MicroRhizon samplers, as well as the extracted DGT-labile P, were determined by an EnSpire microplate reader, PerkinElmer® (Waltham, MA, USA) using miniaturized spectrophotometry methods (Laskov et al., 2007). The sulfate and chloride ion concentrations were determined by ion chromatography (Dionex, ICS 1600, USA).

Some of the sediment samples were immediately centrifuged to remove the porewater. These samples, together with the rest of the samples, were then freeze-dried at −80 °C and ground for further analysis. The mobile P and Fe were extracted by an ascorbic acid solution using a single-step procedure to extract the reactive P pool (ASC-P) bound to amorphous iron and the amorphous iron (ASC-Fe) (Rozan et al., 2002). The measurement of the extracted P and Fe in the eluates was also conducted by the microplate reader. The total nitrogen (TN), total reductive sulfur (TRS, defined as the total sulfur corrected for the sulfate removed by the porewater) and total organic carbon (TOC) were determined by a Vario EL III element analyzer (Elementar, Germany). The particle size was measured by a Mastersizer 3000 (Malvern Instruments Ltd., UK.) using whole samples.

Method blanks, duplicates, and standard materials were used for quality assurance and quality control. Standard materials were measured after every 10 to 20 samples. Three replicate measurements of the TOC, TRS, TN, sulfate and chloride ion were conducted every 10 to 20 samples. Two replicate measurements were performed for the porewater SRP and soluble Fe due to the limited samples. Three replicate measurements were performed for all other samples. The standard materials, average values of the standard material recovery and relative standard deviation (RSD) of the replicates are shown in Table S2.

2.6. Data processing

The accumulated mass (M, μg) of the DGT-labile P was calculated with Eq. (1):

$$M = \frac{C_e V_e}{f_e} \quad (1)$$

where C_e is the measured P concentration in the eluate; V_e is the volume of the eluate; and f_e is the extraction yield.

The accumulated mass (M_S, μg cm^{-2}) of the DGT-labile S was calculated using the calibration curve of the grayscale density (y) versus M_S (x) (Ding et al., 2012):

$$y = -171e^{-x/7.23} + 220 \quad (2)$$

The fluxes of the DGT-labile P/S (F_{DGT}, pg cm^{-2} s^{-1}) and DGT-labile P concentrations (C_{DGT}, mg L^{-1}) were calculated using Eqs. (3) and (4), respectively (Zhang et al., 1995):

$$F_{DGT} = \frac{M}{At} = \frac{M_S}{t} \quad (3)$$

$$C_{DGT} = \frac{M\Delta g}{DAt} \quad (4)$$

where A is the exposure area of the gel strip; t is the deployment time; Δg is the thickness of the diffusive layer (0.08 cm); and D is the diffusion coefficient of P in the diffusion layer (cm^2 s^{-1}) (Wang et al., 2016).

The resupply parameter (R) is calculated as the ratio of the DGT-labile P concentration to the SRP concentration, where a higher value indicates a higher resupply capacity from the sediment to the porewater. The SRP concentrations in the vicinity of the SWI (2 cm above and below) were used to calculate the benthic diffusion flux of SRP between the porewater and overlying water. The flux was calculated based on Fick's first law and the degree of sediment tortuosity according to Boudreau (1996). The correlation analysis of Kendall's Tau was performed using SPSS ver. 13.0.

3. Results

3.1. Properties of sediments and the overlying water

The physicochemical properties of the surface sediments over twelve months are shown in Table 1. The particle size results suggested that silt was the main sediment type, which exhibited seasonal differences (Fig. S3). The C/N value ranged from 8.7 to 11.6, indicating a mixed origin of the OM, which was more thalassogenous overall. Both the monthly distributions and depth profiles of ASC-P and ASC-Fe over the four months were quite consistent (Fig. 1) and increased in summer and decreased in winter. The distributions of TOC and TRS were also coincident with the low contents in winter and fluctuated contents in the other months (Fig. 1).

Table 1
Physicochemical properties of the surface sediments and average values of the P, Fe and S contents in the porewater and DGT profiles in each month.

Month	ASC-P	ASC-Fe	TRS	TOC	C/N	Clay	Silt	Sand	SRP	Soluble Fe	DGT-labile P	DGT-labile S	R
	g kg^{-1}	g kg^{-1}	g kg^{-1}	%		%			mg L^{-1}	mg L^{-1}	pg cm^{-2} s^{-1}	pg cm^{-2} s^{-1}	
2018–5	0.020	1.25	1.44	0.65	9.5	23.96	68.22	7.82	1.13	1.86	27.4	36.9	0.26
2018–6	0.027	1.64	1.03	0.54	11.4	33.78	64.53	1.69	1.80	1.19	21.2	26.1	0.20
2018–7	0.025	1.39	1.61	0.70	9.9	28.62	70.78	0.59	1.64	0.96	47.0	47.3	0.49
2018–8	0.017	0.53	1.16	0.58	11.6	24.64	70.51	4.85	0.34	0.25	22.1	20.8	0.47
2018–9	0.022	1.51	1.89	0.74	11.5	15.86	66.64	17.50	1.08	1.73	77.4	34.0	0.90
2018–10	0.023	0.93	1.56	0.70	8.5	25.90	72.09	2.00	0.78	3.69	39.1	18.5	–
2018–11	0.010	0.62	1.36	0.50	9.8	22.35	69.56	8.09	0.15	3.29	30.3	13.4	1.48
2018–12	0.010	0.58	1.00	0.51	9.5	18.00	68.85	13.15	0.11	2.20	26.4	14.7	1.24
2019–1	0.011	0.79	1.15	0.61	9.0	16.56	65.46	17.98	0.25	1.17	12.3	5.6	0.92
2019–2	0.008	0.69	1.10	0.43	9.1	3.60	74.59	21.81	0.20	0.88	7.9	5.9	1.12
2019–3	0.012	1.00	1.57	0.62	8.7	3.30	84.39	12.31	0.63	1.15	24.6	9.4	1.17
2019–4	0.012	1.31	2.38	1.00	9.0	4.40	81.46	14.14	0.91	1.29	68.1	27.8	0.68

The average SRP concentrations and other properties of the overlying water in each month are presented in Tables 2 and S1. The SRP concentrations were higher in summer and lower in winter. A low salinity was observed in August, March and April, in accordance with the river flood season with intense rainfall (http://en.weather.com.cn/). The dissolved oxygen (DO) concentrations showed some hypoxia, especially in summer and autumn. The overlying water was basically alkalescent with a pH ranging from 7.73 to 8.46.

3.2. Properties of the porewater

The concentrations of SRP and soluble Fe in the overlying water and porewater profiles are shown in Fig. 2. The mean concentrations of the porewater SRP and soluble Fe over the whole year were 0.75 mg L^{-1} and 1.64 mg L^{-1}, respectively, with the highest values observed in June (3.93 ± 0.06 mg L^{-1}) and October (6.17 ± 0.09 mg L^{-1}), respectively. The average SRP concentrations were high in spring and summer (from March to October except August) and low in winter, while the average soluble Fe concentrations were evidently high in autumn (from September to December) (Fig. 8). Although the depth profile varied monthly, the soluble Fe concentration was low in the surface layer and then increased at different depths, mostly followed by a decrease and fluctuation to the bottom. Some SRP profiles had similar patterns, while other profiles began with relatively high concentrations and decreased with depth in the winter (e.g., November and December), which was attributed to the supplied SRP from the overlying water. The Kendall's Tau correlations between the SRP and soluble Fe concentrations in the depth profiles were variable, with no positive, significant negative and no positive or negative correlations in the different months (Fig. 2). The sulfate concentrations mainly decreased with depth and were the lowest in July, while the chloride ion/sulfate ratio stably increased with depth and was highest in July.

3.3. Properties of the DGT-labile P and DGT-labile S

The two-dimensional (2D) monthly heat maps of the DGT-labile S distributions, as shown in Fig. 3, present remarkable spatiotemporal changes with overall high values and high horizontal heterogeneity in the spring and summer. The one-dimensional (1D) depth distributions of DGT-labile S converted from the 2D images and DGT-labile P distributions (Fig. 4) showed synchronous variation trends with significant positive correlations in most profiles except in January, February and March, which are characterized by the lowest DGT-labile S fluxes. The average DGT-labile P concentrations were insufficient compared with the DGT-labile S in May, June and July, while the DGT-labile P exhibited consistent changes with the DGT-labile S in the other months (Fig. 8). In the vertical distributions of DGT-labile S/P, the lowest values occurred in the uppermost or subsurface layer, and the values continued to rise and then declined, or alternately increased and decreased, accompanied by fluctuations to various degrees. All the data in July and October were cited from Pan et al. (2019a).

3.4. Changes in P, Fe and S during the indoor experiments

In the experimental group, as shown in Fig. 5A, the SRP and soluble Fe concentrations were lowest at 1 cm depth, and they both rapidly increased in the next 2 cm, followed by a slight and fluctuating increase to the bottom. Their changes with time presented prominent and moderate tidal patterns (with higher values during flood tides and lower values during ebb tides) at 1 cm and 2 cm depth, respectively, and an irregular tidal pattern at 3 cm depth. In the control group, as shown in Fig. 5B, the depth distributions of SRP and soluble Fe were variable and irregular, characterized by an apparent decrease in SRP with time. The changes in soluble Fe with time at shallow depths showed patterns similar to those in the experimental group, while SRP showed a remarkable tidal pattern at all depths.

In the experimental group, as shown in Fig. 6, the DGT-labile S fluxes during flood tides were higher than those during ebb tides with rapid increases in both at approximately 12 cm depth. Although a positive correlation was observed between the DGT-labile P and DGT-labile S, their distribution trends are not uniform, especially the high DGT-labile P fluxes accompanied by the nearly undetectable DGT-labile S at a depth of 10 cm. In the control group, the tidal pattern of the DGT-labile S was more distinct with generally higher fluxes and shallower depths of the peak values during both flood tides and ebb tides. The synchronous distributions between the DGT-labile P and DGT-labile S were more significant; a consistent tendency of high values for both parameters during flood tides and low values for both parameters during ebb tides was also observed.

3.5. Diffusion fluxes of the SRP across the SWI

The benthic diffusion fluxes of SRP across the SWI, as shown in Fig. 7, were positive (from the porewater to the overlying water) only in May, June and April, negative (from the overlying water to the porewater) in most months and blank in July and October due to insufficient data. The highest positive flux occurred in May (1.23 mg m^{-2} d^{-1}), while the highest negative flux occurred in September (5.34 mg m^{-2} d^{-1}). The overall trend of SRP diffusion during the whole year was from the overlying water to the porewater. We assume that each flux represents the value for each

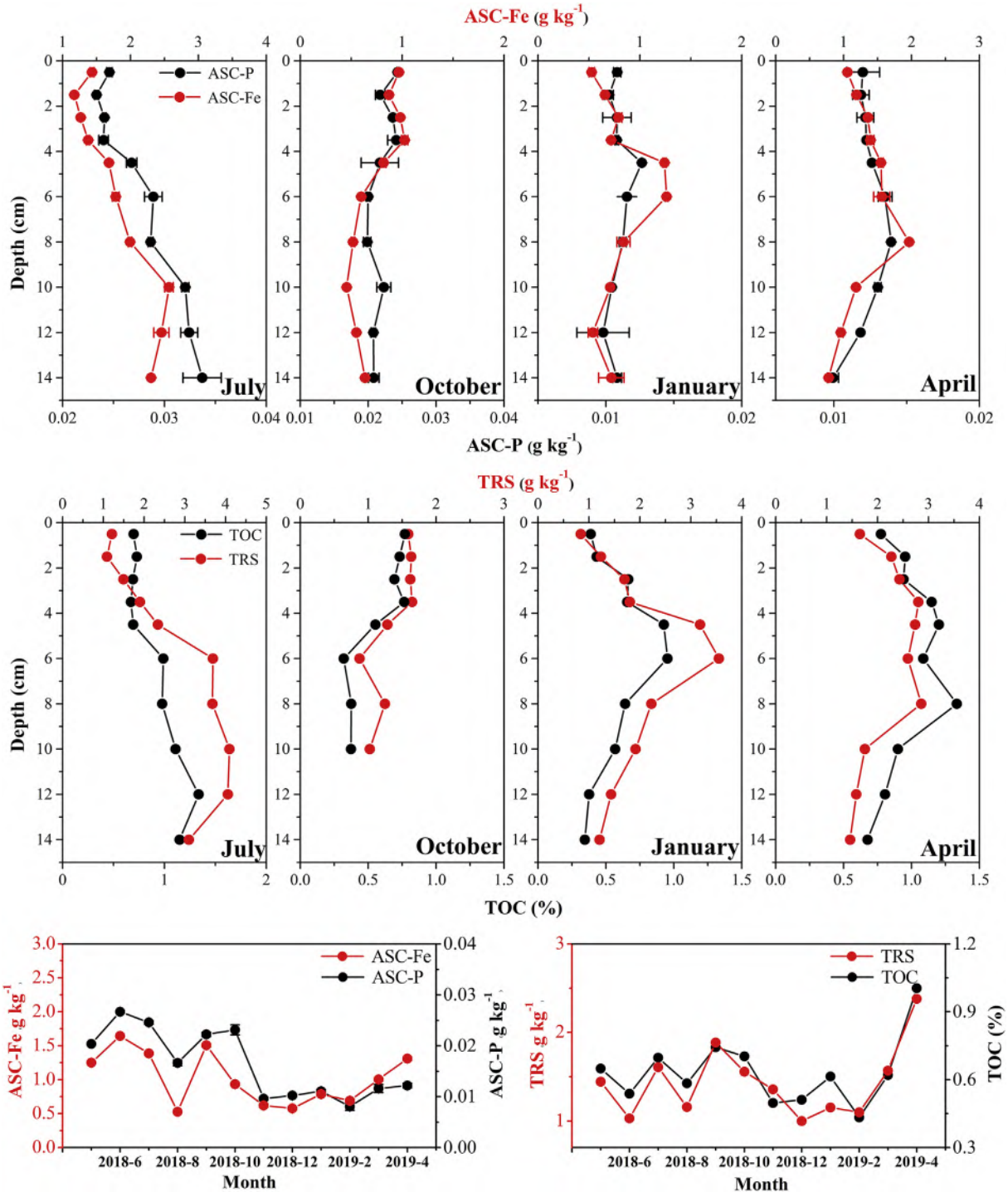

Fig. 1. Depth profiles of the ASC-Fe, ASC-P, TRS and TOC contents in the sediment cores over four seasons and their average values in the surface sediments over twelve months.

month, and the average flux in the whole year can be calculated as −0.580 mg m^{-2} d^{-1}.

4. Discussion

4.1. Holistic assessment of P mobility and pollution

Compared with the defined National Surface Water Environmental Quality Standards (GB 3838-2002) and the Sea Water Quality Standard (GB 3097-1997) in China, as well as the quality standard for surface waters set by the Council of the European Communities (75/440/EEC) as shown in Table 2, the overlying water SRP concentrations exceeded different grades (mostly grade III) of threshold values from GB 3838-2002, the supreme grade IV threshold values (0.045 mg L^{-1}) from GB 3097-1997 in all months, and the indicator level (0.1 mg L^{-1}) for possible problematic algal growth from 75/440/EEC in most months. The SRP concentrations were also obviously higher than those in the adjacent Jiulong River Estuary (0.075 mg L^{-1} (Pan et al., 2019b)) and Xixi Estuary (~0.1 mg L^{-1}, unpublished results) around Xiamen Bay. These

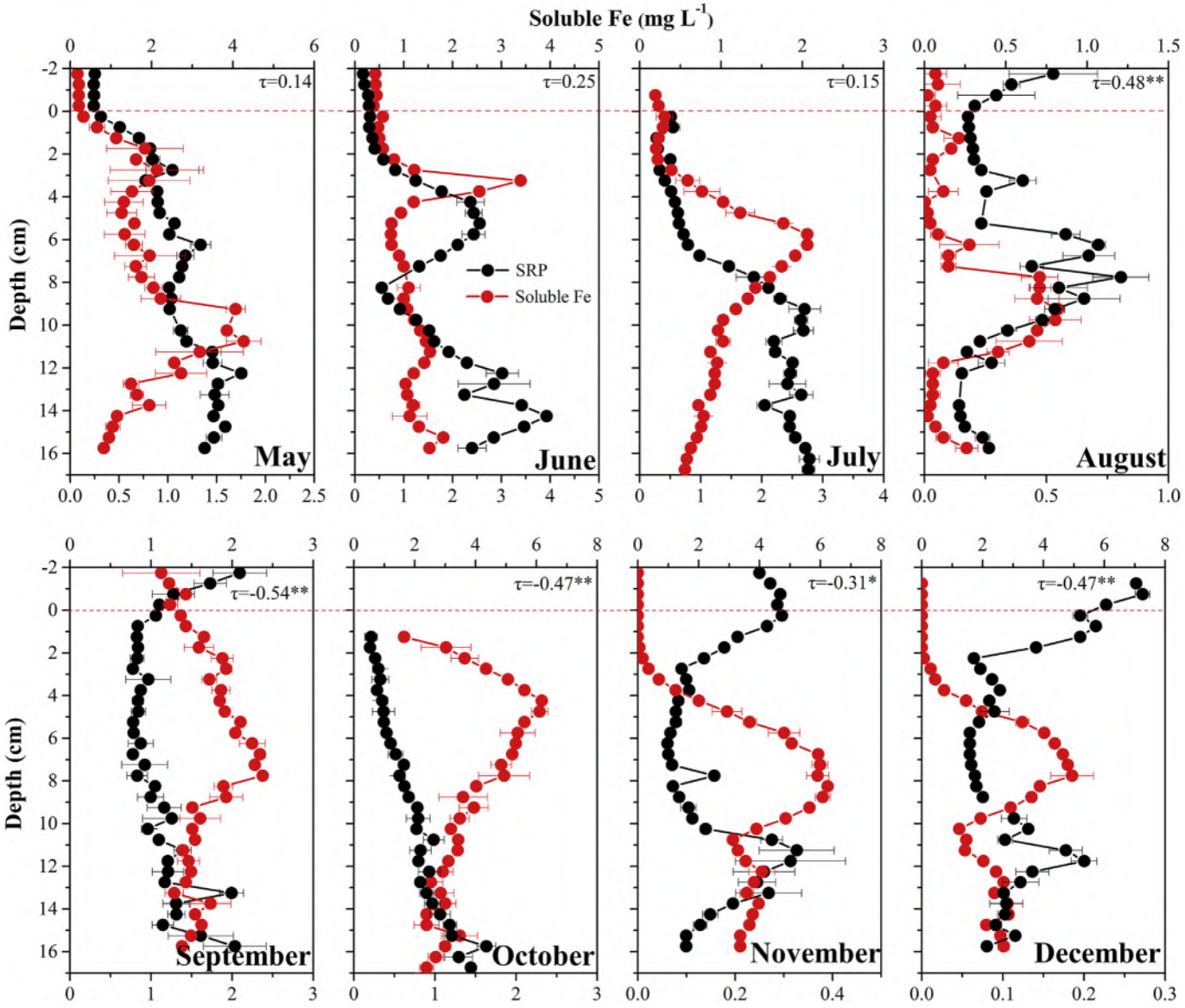

Fig. 2. Monthly distributions of the SRP, soluble Fe, sulfate and chloride ion (presented here as the chloride ion/sulfate ratio) concentrations in the overlying water-porewater profiles sampled by the HR-Peeper probes. The sulfate and chloride ion concentrations were measured in only three months. The results indicate Kendall's Tau correlations between the soluble Fe and SRP at the >95% confidence level, with ** denoting significance at the $p < 0.01$ level and * denoting significance at the $p < 0.05$ level. The same applies below (Figs. 4 and 6). The red dashed line denotes the SWI, above which is the overlying water and below which is the porewater. (For interpretation of the references to colour in this figure legend, the reader is referred to the Web version of this article.)

results indicate relatively inferior water quality and alarming P pollution in the Jiuxi River Estuary throughout the year, and this pollution can be transported to the adjacent Xiamen Bay and promote its subsequent eutrophication.

The concentrations of overlying water SRP, porewater SRP and sediment ASC-P were high in spring and summer and low in winter (Figs. 1 and 8), suggesting that intense P mobilization and pollution occurred in spring and summer, which were consistent with high diffusion fluxes (Fig. 7). A previous study found that algal blooms in the Xiamen Sea area were generally severe in spring (Yang et al., 2012). Hence, the positive fluxes in spring (April, May and June) may act as crucial internal P loading to promote algal blooms and create a positive productivity feedback that results in deterioration of the water quality. When the algae degrade afterwards in summer and autumn, the highest concentrations of overlying water SRP occurred and migrated back into the porewater with the highest negative fluxes (Fig. 8), which subsequently functioned as reactive P pools for future remobilization. During winter, however, all of the above parameters declined, while high concentrations and R values of the DGT-labile P were still sustained (Fig. 8 and Table 1). This result indicates a strong capacity of the sediment to resupply porewater and thus a high liberation risk to the overlying water is still present.

4.2. Seasonal changes in sulfate reduction and Fe(III) reduction and their effects on P mobility

The sulfate concentrations and chloride ion/sulfate ratios in Fig. 2 clearly reveal that the degrees of sulfate consumption are in line with the DGT-labile S fluxes and have not been limiting factors

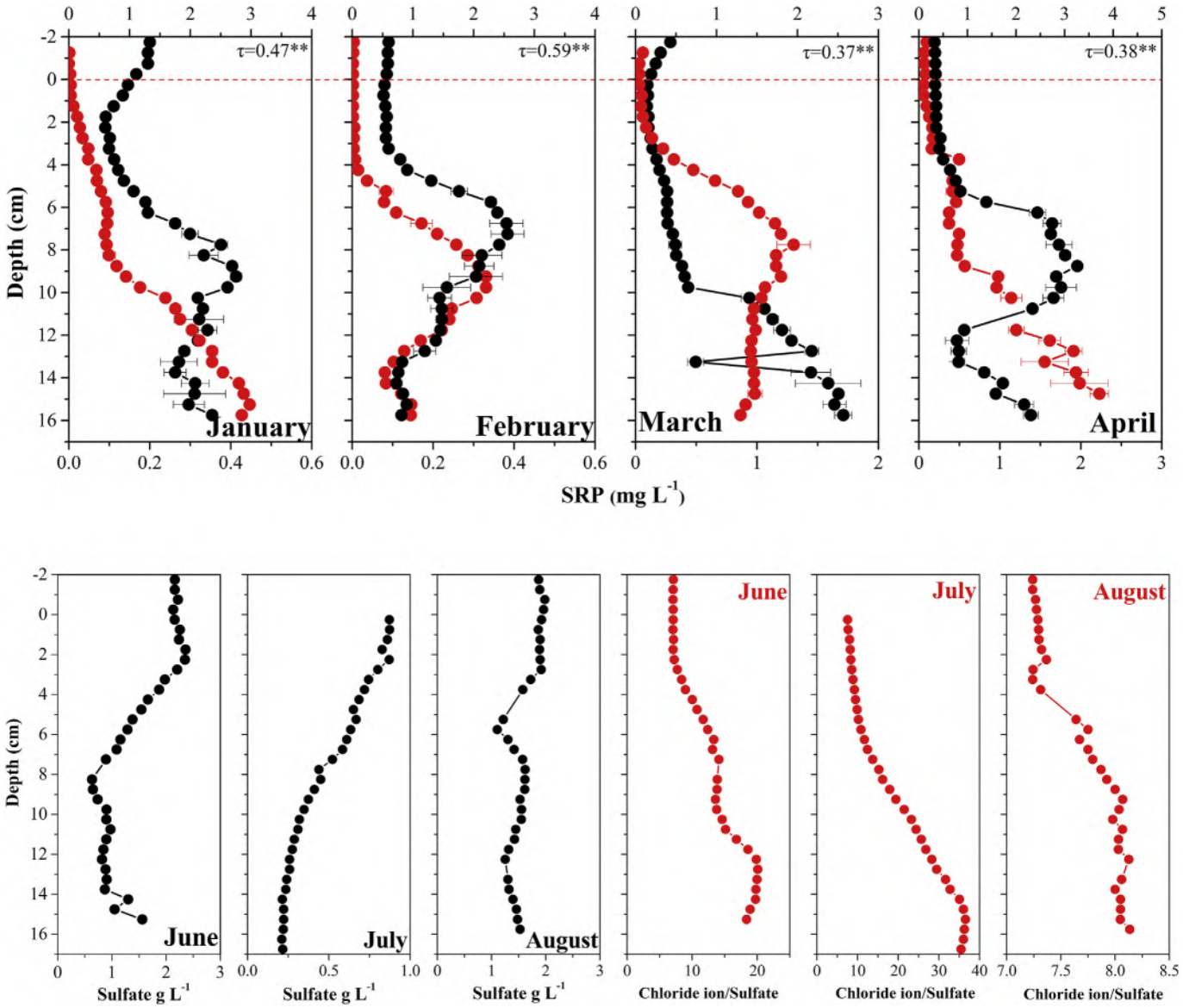

Fig. 2. (*continued*).

for the intense DSR, even in the deep sediments in July (Fig. 3). The DGT-labile S fluxes increased in spring and summer and decreased in autumn and winter (Figs. 3 and 8), demonstrating that the DSR rates and sulfide production are highly temperature-dependent, possibly due to thermophilic sulfate-reducing bacteria (van Bodegom and Stams, 1999). Relatively low TOC contents may also restrict DSR in winter (Bottrell et al., 2009). The significant positive correlations between the DGT-labile S and DGT-labile P in most months (Fig. 4) indicate a vigorous control of the intense DSR and dissolved sulfide on P mobilization and release via both anaerobic organic P mineralization and sulfide-induced reductive dissolution of the Fe-bound P (Ding et al., 2012; Markovic et al., 2019; Moses and Herman, 1991). Nevertheless, the control and correlations become weak when the DSR rates decline in winter (January, February and March, Fig. 4), suggesting that less DSR and sulfide production results in a decreased control on P mobilization and distribution in winter.

DIR and DSR compete as electron acceptors during OM diagenetic mineralization (Gonzalez-Silva et al., 2009), while DSR commonly gains an advantage over DIR and restricts soluble Fe distributions in coastal sediments (Muyzer and Stams, 2008) due to sufficient OM and sulfate in surface sediments. The aforementioned is generally in accordance with this study, which is characterized by high DGT-labile S fluxes compared with a previous study in the adjacent Jiulong River Estuary (Pan et al., 2019c) and subnormal soluble Fe concentrations in spring and summer (Fig. 8). This result signifies that intense DSR in spring and summer dramatically suppresses DIR and removes soluble Fe from the porewater by coprecipitation. The highest soluble Fe concentrations occurred in autumn when DSR declined with the temperature and thus its restriction on DIR was weakened.

Fe(III) (hydr)oxides are known to exert vital control on P mobility by scavenging SRP through strong absorption (the consistent spatiotemporal distributions of ASC-Fe and ASC-P in Fig. 1) and reductive dissolution to release SRP (Kraal et al., 2015; Rozan et al., 2002), resulting in low concentrations in oxic porewater and increasing concentrations in the iron-reducing zone for both SRP and soluble Fe (Ding et al., 2018). However, the generally inconsistent distributions and weak positive correlations between SRP and soluble Fe (Fig. 2), as well as the exceptionally high SRP

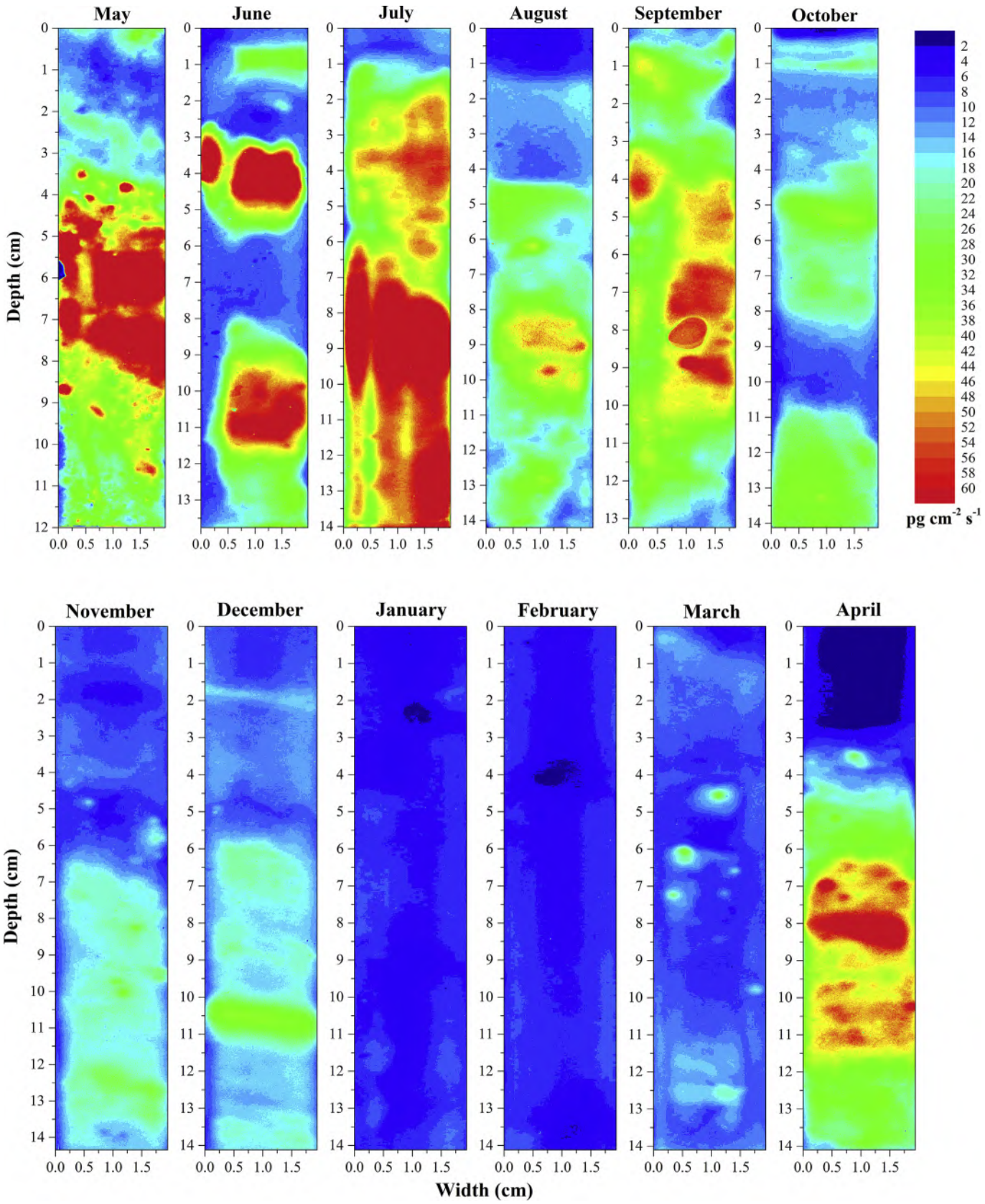

Fig. 3. Two-dimensional monthly DGT-labile S distribution heat maps measured by the DGT probes.

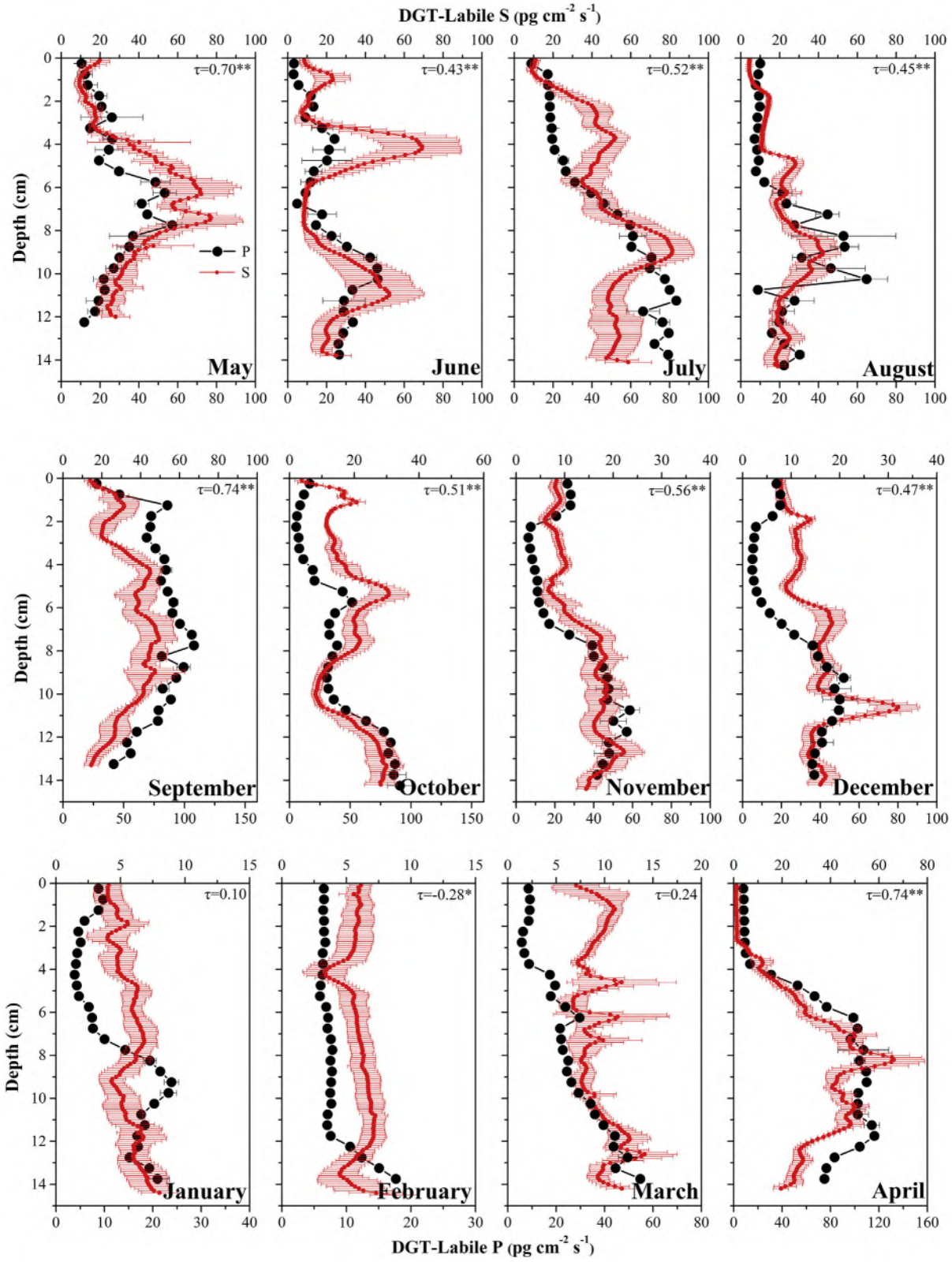

Fig. 4. Synchronous DGT-labile P and DGT-labile S one-dimensional depth profiles measured by one DGT probe. The DGT-labile S curves were converted from the 2D images in Fig. 3 using average horizontal data with a resolution of 1 mm in the vertical direction. The horizontal heterogeneity is reflected by the error bars.

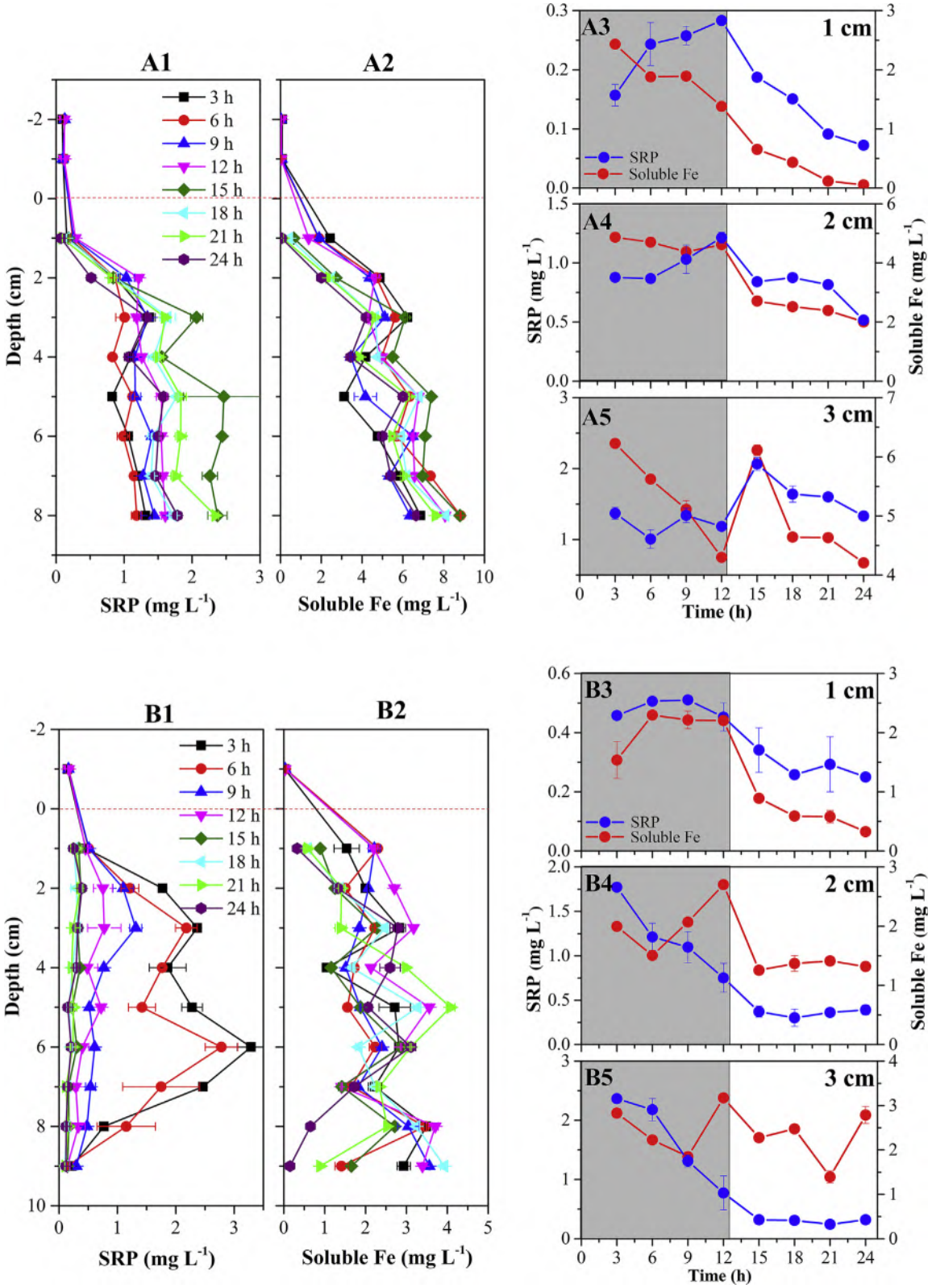

Fig. 5. Depth profiles of the SRP and soluble Fe sampled by MicroRhizon samplers during the indoor experiments (A1, A2, B1 and B2) and their changes with time at shallow depths (A3, A4, A5, B3, B4 and B5). The gray and blank areas in A3, A4, A5, B3, B4 and B5 denote the flood tides and ebb tides, respectively. The figure A series denotes the experimental group, while the figure B series denotes the control group.

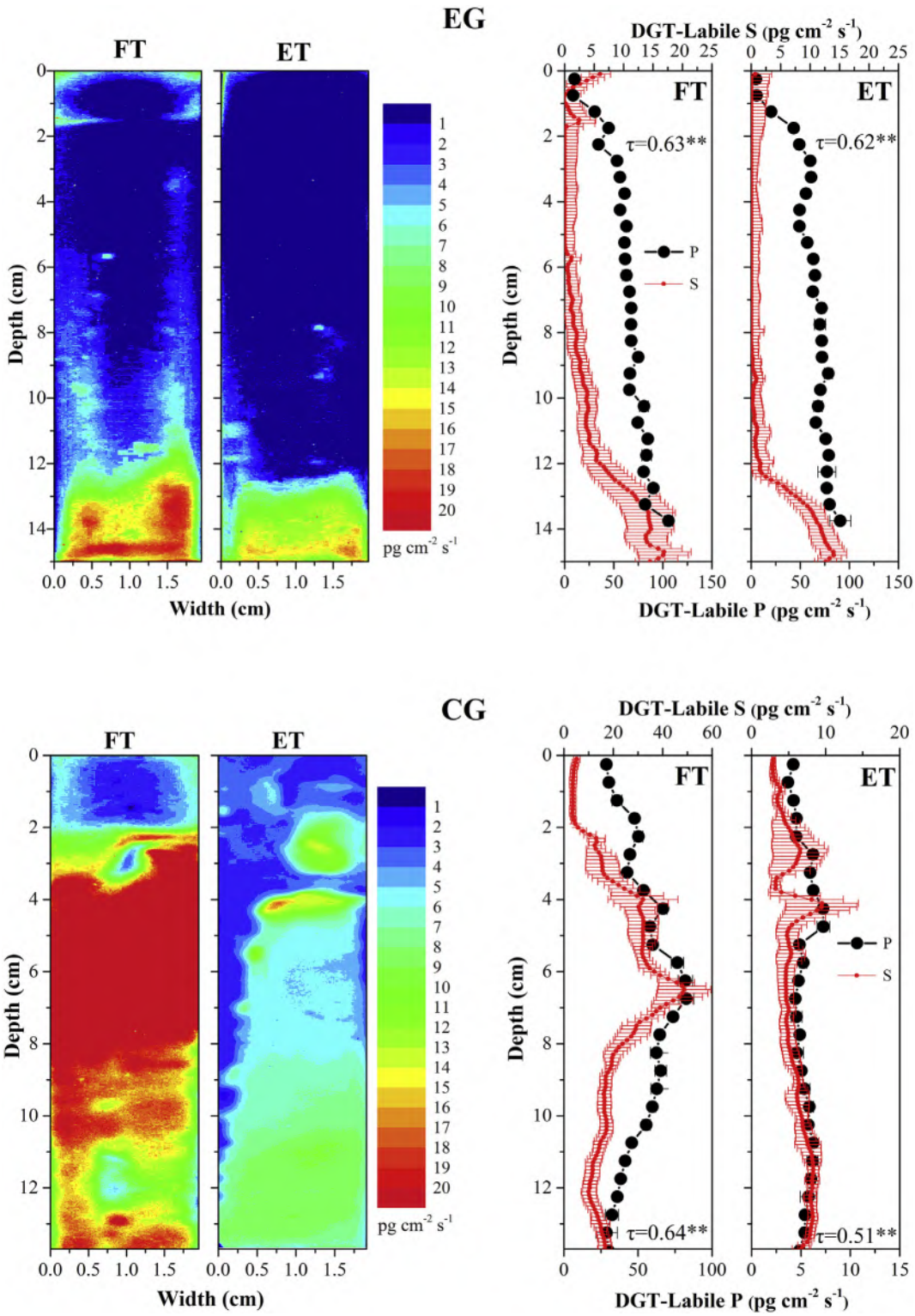

Fig. 6. 2D distributions of the DGT-labile S and 1D depth profiles of DGT-labile S and P during the indoor simulations of the flood tides (FT) and ebb tides (ET) in the experimental group (EG) and control group (CG).

concentrations beyond the suprathreshold values (Fe:P molar ratio of 2:1) of P-ferrihydrite assemblages (Thibault et al., 2009) in most profiles, demonstrate that Fe redox geochemistry is no longer the dominant factor controlling P mobility in most months. This change should be explained by the disturbance of DSR and concomitant sulfide to restrain DIR, coprecipitate with soluble Fe, cause chemical reductive dissolution of Fe(III) (hydr)oxides that diminishes P sequestration capacity and mobilize reactive organic P (Ingall and Jahnke, 1997; Middelburg and Levin, 2009; Xiong et al., 2019), leading to partial removal of soluble Fe and additional SRP

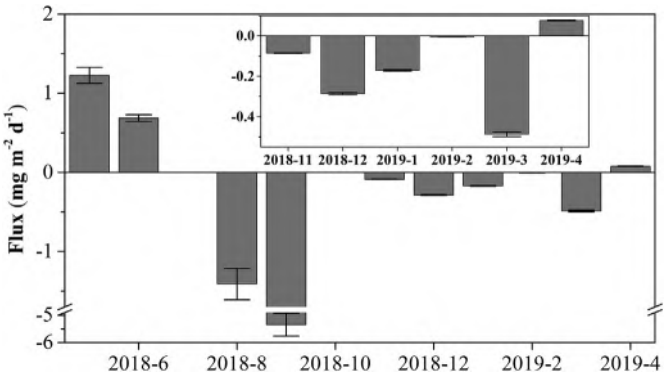

Fig. 7. Benthic diffusion fluxes of SRP across the SWI, with the positive values denoting the net fluxes from the porewater to the overlying water and the negative values denoting the net fluxes from the overlying water to the porewater.

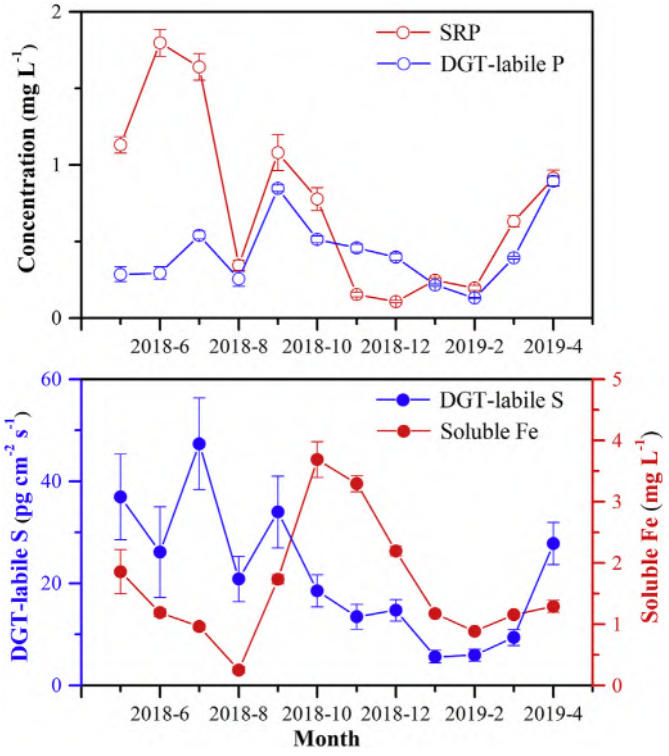

Fig. 8. Monthly changes in the average SRP, DGT-labile P, DGT-labile S and soluble Fe concentrations in the sediment/porewater profiles in a whole year.

production. However, due to the declining DGT-labile S in the winter (January and February), Fe cycling seems to control P mobility, as evidenced by the significant positive correlation between the soluble Fe and SRP and the exceptional inconsistent distributions between the DGT-labile S and P (Figs. 2 and 4, respectively).

In addition, taking the monthly average values as an example, the SRP concentrations showed significant positive correlations with the ASC-P/Fe contents, while the DGT-labile P concentrations showed significant positive correlations with the TOC and TRS contents (Fig. S4). The former result indicates that although P retention is dominated by Fe(III) (hydr)oxides (Rozan et al., 2002), the solidified Fe-bound P can act as an important pool for P remobilization (Ding et al., 2015); the latter phenomenon demonstrates that the labile P in sediment is tightly coupled with DSR as TOC and TRS basically represent the substrate and product of DSR, respectively, further implying that DSR is a crucial process to improve the P mobility and the resupply capacity for persistent remobilization and liberation, respectively. The coupling relationship between TOC and TRS (Fig. 1) also demonstrates that the accumulation of (poly)sulfide may be facilitated by the OM burial associated with expanding hypoxic marine conditions (Raven et al., 2016, 2019).

4.3. Circannual cyclical pattern of P and the underlying mechanisms

As the major sensitive indicators reflecting P mobility in sediments, the SRP and DGT-labile P concentrations exhibited different monthly/seasonal changes, with the highest values in June and July for SRP and in September and April for DGT-labile P, and the lowest values in the winter for both parameters (Fig. 8). Based on the monthly changes in SRP and DGT-labile P, as well as the Fe and S cycling discussed in section 4.2 and other environmental factors, the underlying mechanisms responsible for the monthly/seasonal P (im)mobilization are discussed below (illustrated in Fig. 9).

4.3.1. May, June and July

DSR greatly suppressed DIR and dominated P mobilization via OM mineralization and chemical reductive dissolution of the Fe-bound P, resulting in the highest porewater SRP concentrations (Fig. 8) and thus considerable diffusion fluxes to the overlying water (Fig. 7). Nevertheless, the DGT-labile P concentrations and especially the R values were unstable even though the DGT-labile P exhibited tight coupling with the DGT-labile S. This phenomenon could be explained by the high ASC-Fe contents that have not been completely consumed by microbial/chemical reduction, thus sustaining a high P sequestration ability (Lin et al., 2017) and persistent SRP diffusion to the overlying water, which greatly weakens the desorption and resupply capacities of the sediment labile P (Ernstberger et al., 2005).

4.3.2. August

A week of heavy rain occurred in the beginning of August, leading to a rising water level, especially during low-tide times. Pan et al. (2019c) have confirmed that enhanced anaerobic P mobilization and migration to the overlying water can occur under hypoxic conditions during the flood season, leading to rapid labile P exhaustion in a short period. This phenomenon was in accordance with the pronounced decreases in the SRP, DGT-labile P and ASC-P concentrations in this study when sampling was conducted after the flood season. Moreover, sampling coincided with the astronomical tide (exceeding 5.5 m) characterized by nearly evaporated overlying water during low-tide time, thereby maintaining a relatively well-oxygenated surface layer to restrain DIR and DSR with valley values until approximately 6 or 4 cm depth, respectively (Figs. 2 and 3). Due to the preceding P consumption and SRP diffusion from the overlying water to the sediment, combined with the decreased ASC-Fe, the P resupply from the sediment is promoted to obtain the observed high DGT-labile P concentrations and R values.

4.3.3. September, October, November and December

In September, the increased TOC input from algal degradation promoted DSR and DIR, while the continual and considerable SRP supplementation from the overlying water (Fig. 7) caused considerable DGT-labile P concentrations. During the dry season of autumn, DSR still dominated P mobilization, although the rates gradually decreased with decreasing temperature. DIR was rapidly increased, and ASC-Fe/P was constantly consumed, which also

Table 2
Comparison of the overlying water SRP concentrations in each month with defined standards.

Month	Overlying water SRP (mg L^{-1})	Ratio to the criterion value		
		GB3838−2002	GB 3097-1997	75/440/EEC
2018−5	0.245	1.23 III	5.44 IV	2.45
2018−6	0.231	1.16 III	5.13 IV	2.31
2018−7	–	–	–	–
2018−8	0.347	1.16 IV	7.71 IV	3.47
2018−9	1.55	3.88 V	34.4 IV	15.5
2018−10	–	–	–	–
2018−11	0.275	1.38 III	6.11 IV	2.75
2018−12	0.255	1.28 III	5.67 IV	2.55
2019−1	0.190	1.90 II	4.22 IV	1.90
2019−2	0.088	4.40 I	1.96 IV	0.88
2019−3	0.197	1.97 II	4.38 IV	1.97
2019−4	0.200	1.00 III	4.44 IV	2.00

The superscript Roman numerals denote the grade of the overlying water SRP; the value is the ratio of the SRP concentration to the corresponding criterion value.

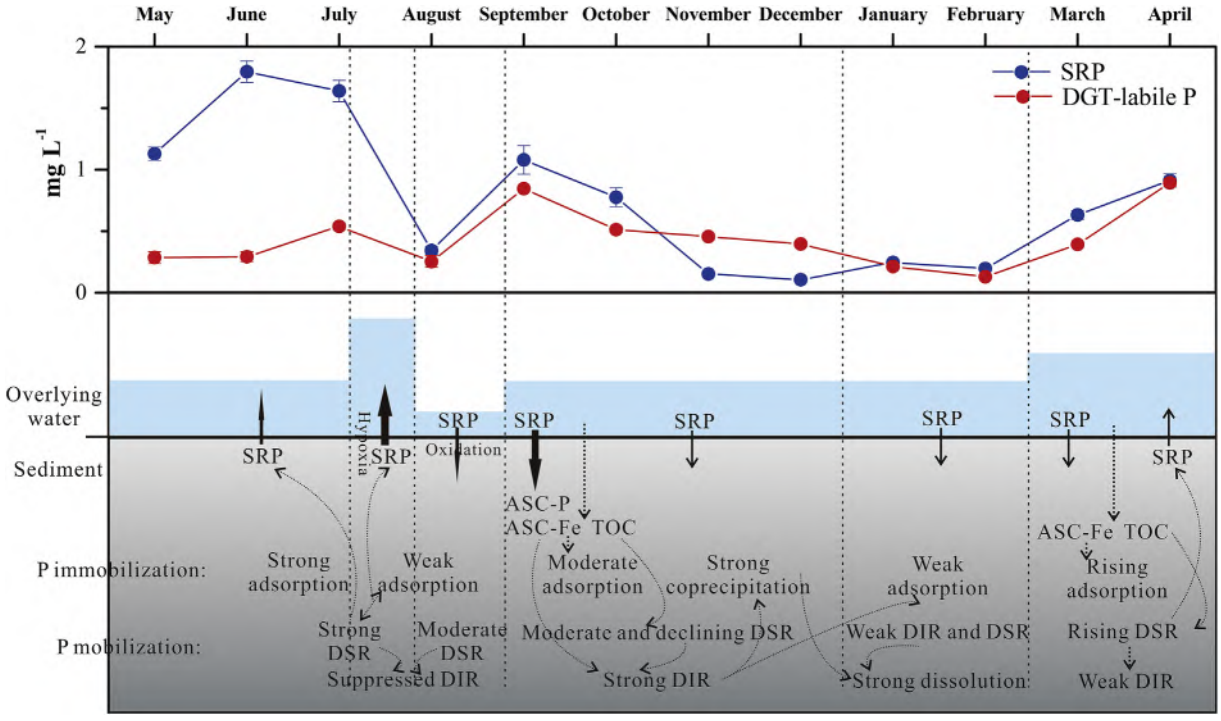

Fig. 9. Illustration of the mechanisms of the monthly/seasonal changes in P mobility in the Jiuxi River estuarine sediments. The thickness of the solid arrow across the SWI for SRP denotes the magnitude of the diffusion flux; The height of the blue area denotes the relative water level influenced by runoff and tide; P immobilization includes adsorption by Fe(III) (hydr)oxides (presented as adsorption in the figure) and coprecipitation with Fe^{2+} (presented as coprecipitation in the figure); P mobilization includes DSR, DIR and dissolution from labile vivianite (presented as dissolution in the figure). (For interpretation of the references to colour in this figure legend, the reader is referred to the Web version of this article.)

facilitated P mobilization. With the high ASC-P and TOC consumption levels in November, the SRP concentrations rapidly declined with moderately decreased DGT-labile S and soluble Fe concentrations. However, although intensive DIR may contribute greatly to P mobilization, the prominent increased soluble Fe, and existing high SRP concentrations appear to exceed concentration thresholds that can trigger noteworthy Fe−P authigenic minerals (e.g., vivianite) (Nriagu, 1972). Vivianite has been widely found and described in marine sediments in recent years (Egger et al., 2015; Marz et al., 2018; Xiong et al., 2019). The presence of vivianite is verified by the significant negative correlations between SRP and soluble Fe, especially the declined SRP concentrations accompanied by peak values of the soluble Fe (Fig. 2). In addition to the continual SRP supplementation from the overlying water and conspicuously consumed ASC-Fe (Figs. 7 and 1), the presence of vivianite is also the key reason to explain the surprising R values (above 1) in November and December via the established precipitation equilibrium of vivianite, whereby SRP supersaturation of the porewater occurs via resupply, which is captured by DGT.

4.3.4. *January and February*

In winter, both the DSR and DIR rates decrease, especially DSR with the lowest DGT-labile S fluxes, leading to weak P mobilization with valley levels for both SRP and DGT-labile P (Fig. 8). Dissolution of mobile vivianite may be the dominant P source for porewater, resulting in elevated SRP concentrations that occur in the porewater as the soluble Fe concentrations decrease through weak DIR. The still high R values are due to reasons that are analogous to those for November and December.

4.3.5. March and April

With the temperature and precipitation rising in spring, as well as the increased runoff and TOC input, intense DSR is resumed and dominated P mobilization, leading to overall mounting SRP and DGT-labile P concentrations (Figs. 2 and 4). However, the elevated ASC-Fe contents from terrigenous input can restrain P mobility by detention as ASC-P in surface layers (Fig. 1), thus sustaining low concentrations of mobile P concentrations, which also explains the decreased R value (0.68) in the surface layer in April.

On the whole, the seasonal changes in DSR and S redox cycling are the main internal drivers for P mobilization and release, while DIR and Fe cycling have been widely accepted in previous studies (Kraal et al., 2015; Pan et al., 2017; Xu et al., 2012). This is the first time that visible evidence of coupled labile P–S (Fig. 4) has been provided to clarify the spatiotemporal domination of DSR on P mobilization in estuarine sediments. In addition, previous estuarine and coastal studies have revealed that temperature-induced seasonal changes in the redox environment are the main external factor controlling P cycling via changed Fe and S cycling (Liu et al., 2018; Pan et al., 2019c; Rozan et al., 2002). However, in this study, we emphasize that in addition to temperature, monthly changes in runoff and tidal range are crucial external factors to control long-term P cycling via changed redox environments and terrigenous material inputs. This research demonstrates the significance and necessity of high-resolution spatiotemporal field study for summarizing the circannual pattern of P, which should reasonably consider the spatiotemporal variations in important environmental factors.

4.4. Verification of the tide-induced P, Fe and S changes by the indoor experiments

Recently, Pan et al. (2019c) revealed that the DGT-labile S in intertidal surface sediments exhibits a prominent tidal pattern with higher values during flood tides and lower values during ebb tides in field studies. Our indoor experiments thoroughly verify the previous field observations of DGT-labile S enrichment and consumption explained by hypoxia-fueled DSR and sulfide reoxidation during the tidal cycle (Fig. 6). Furthermore, we find, for the first time, that the soluble Fe, SRP and DGT-labile P also present similar tidal patterns during indoor experiments (Figs. 5 and 6), demonstrating that the short-term cycling of P, Fe and S in intertidal surface sediments is highly redox-sensitive and is controlled by tidal processes.

In the experimental group, the mixing and oxidization of sediment successfully suppressed DSR until a depth of 12 cm and weakened the consistent distributions between DGT-labile S and P (Fig. 6). However, the high soluble Fe concentrations and significant positive correlations with SRP at all times (Fig. S5) suggest that oxidization slightly affected DIR, resulting in intense DIR without restriction by DSR to dominate P mobilization till at least a depth of 8 cm. In addition, both soluble Fe and SRP showed tidal patterns at a depth of 2 cm (Fig. 5A), further indicating that the domination of P mobilization and the relevant tidal pattern are controlled by Fe cycling. In the control group of undisturbed sediment, a high DGT-labile S flux occurred below the 2 cm depth during flood tides and rapidly decreased during ebb tides (Fig. 6), accompanied by consistent DGT-labile P and SRP distributions (Figs. 5B and 6), as well as irregular and declined soluble Fe concentrations, demonstrating that DSR effectively suppressed DIR and dominated P mobilization. This finding was further confirmed by the weak correlations between the soluble Fe and SRP (Fig. S6). Under these circumstances, the tidal pattern of P occurring at all shallow depths (Fig. 5B) is also attributed to a change in DSR, while the soluble Fe showed a tidal pattern only at a depth of 1 cm.

Overall, the indoor experiments further verify the leading role of DSR in OM mineralization and P mobilization while suppressing DIR. In addition, the tidal pattern of DSR and associated P mobilization are remarkable, which may induce intensive periodic P liberation to the overlying water (high values of SRP and DGT-labile P in the surface layers during flood tides, Figs. 5B and 6). However, treatment by sediment oxidization can effectively restrain DSR and convert to a DIR-dominated system. Unlike DSR, the tidal pattern of DIR and associated P mobilization are moderate and sustain relatively low SRP and DGT-labile P concentrations in the surface layers even during flood tides (Figs. 5A and 6). However, against the background of accelerated global changes such as sea level rise, climate change and anthropogenic activities that might result in expanding marine hypoxic conditions, together with the increased OM and external P input, the challenge of enhanced internal P loading in estuaries and coasts is severe, and more attention must be paid to this issue.

5. Conclusions

This study provided detailed insights into the monthly/seasonal P mobility and pollution in dynamic estuarine sediments and further clarified the underlying mechanisms of P (im)mobilization. The overlying water analyses indicate a relatively inferior water quality and alarming P pollution throughout the year, which are closely related to internal P cycling, especially in spring and summer with high diffusion fluxes (both positive and negative). In spring and summer, intense DSR dominated P mobilization via OM mineralization and chemical reductive dissolution of the Fe-bound P; moreover, DSR suppressed DIR and consumed the soluble Fe by coprecipitation with sulfide. This process may be enhanced during the river flood season, resulting in substantial P mobilization and liberation to the overlying water; In autumn, the DSR rates gradually decreased with decreasing temperature, and thus DIR rapidly increased with high soluble Fe concentrations, leading to noteworthy Fe–P authigenesis minerals (e.g., vivianite) and declining SRP concentrations; However, labile vivianite can act as a vital P source in winter via the precipitation equilibrium to resupply SRP and DGT-labile P as the soluble Fe concentrations decreased due to weak DIR. In the following spring with increased runoff and TOC input, intense DSR resumed and dominated P mobilization, leading to increasing SRP and DGT-labile P levels. This circannual cyclical pattern of P indicates that DSR and S redox cycling are the main internal drivers for P mobilization, while monthly changes in runoff and tidal range are crucial external factors to control long-term P cycling via changed redox environments and terrigenous materials inputs.

The soluble Fe, SRP and DGT-labile P/S presented remarkable tidal patterns in the indoor experiments (with higher values during flood tides and lower values during ebb tides), demonstrating that the short-term cycling of P, Fe and S in intertidal surface sediments is highly redox-sensitive and is controlled by tidal processes. The indoor experiments combined with the monthly field observations suggest that intense DSR (both long-term and short-term) greatly facilitates P mobility and release, while dominant DIR and Fe cycling can effectively control P immobilization. Treatment by sediment oxidization can effectively restrain DSR and convert to a DIR-dominated system. Therefore, in addition to controlling external OM and P inputs, we emphasize that extensive sediment oxidation can play a crucial role in controlling the internal P loading in estuarine sediments.

Declaration of competing interest

The authors declare that they have no known competing

financial interests or personal relationships that could have appeared to influence the work reported in this paper.

Acknowledgments

This work was supported by the National Natural Science Foundation of China (Grant No. 41672226). The authors wish to thank Professor Hao Zhang from Lancaster University, Professor Yue Gao from de Vrije Universiteit and Professor Jun Luo from Nanjing University for their technical guidance on the DGT technique at the Kunming conference, 2018. We would also like to thank Kaige Zhao from the Analyzing and Testing Center of Xiamen University for her assistance in quality control and quality assurance during sample analysis.

Appendix A. Supplementary data

Supplementary data to this article can be found online at https://doi.org/10.1016/j.watres.2020.115479.

References

Bottrell, S.H., Mortimer, R.J.G., Davies, I.M., Harvey, S.M., Krom, M.D., 2009. Sulphur cycling in organic-rich marine sediments from a Scottish fjord. Sedimentology 56, 1159–1173. https://doi.org/10.1111/j.1365-3091.2008.01024.x.

Boudreau, B.P., 1996. The diffusive tortuosity of fine-grained unlithified sediments. Geochem. Cosmochim. Acta 60, 3139–3142. https://doi.org/10.1016/0016-7037(96)00158-5.

Cao, X., Liu, X., Zhu, J., Wang, L., Liu, S., Yang, G., 2017. Characterization of phosphorus sorption on the sediments of Yangtze River Estuary and its adjacent areas. Mar. Pollut. Bull. 114, 277–284. https://doi.org/10.1016/j.marpolbul.2016.09.026.

Conley, D.J., Humborg, C., Rahm, L., Savchuk, O.P., Wulff, F., 2002. Hypoxia in the Baltic Sea and basin-scale changes in phosphorus biogeochemistry. Environ. Sci. Technol. 36, 5315–5320. https://doi.org/10.1021/es025763w.

Conley, D.J., Paerl, H.W., Howarth, R.W., Boesch, D.F., Seitzinger, S.P., Havens, K.E., Lancelot, C., Likens, G.E., 2009. ECOLOGY controlling eutrophication: nitrogen and phosphorus. Science 323, 1014–1015. https://doi.org/10.1126/science.1167755.

Davison, W., Zhang, H., 1994. In-situ speciation measurements of trace components in natural-waters using thin-film gels. Nature 367, 546–548.

Diaz, R.J., Rosenberg, R., 2008. Spreading dead zones and consequences for marine ecosystems. Science 321, 926–929. https://doi.org/10.1126/science.1156401.

Ding, S., Chen, M., Gong, M., Fan, X., Qin, B., Xu, H., Gao, S., Jin, Z., Tsang, D.C.W., Zhang, C., 2018. Internal phosphorus loading from sediments causes seasonal nitrogen limitation for harmful algal blooms. Sci. Total Environ. 625, 872–884. https://doi.org/10.1016/j.scitotenv.2017.12.348.

Ding, S., Han, C., Wang, Y., Yao, L., Wang, Y., Xu, D., Sun, Q., Williams, P.N., Zhang, C., 2015. In situ, high-resolution imaging of labile phosphorus in sediments of a large eutrophic lake. Water Res. 74, 100–109. https://doi.org/10.1016/j.watres.2015.02.008.

Ding, S., Sun, Q., Xu, D., Jia, F., He, X., Zhang, C., 2012. High-resolution simultaneous measurements of dissolved reactive phosphorus and dissolved sulfide: the first observation of their simultaneous release in sediments. Environ. Sci. Technol. 46, 8297–8304. https://doi.org/10.1021/es301134h.

Egger, M., Jilbert, T., Behrends, T., Rivard, C., Slomp, C.P., 2015. Vivianite is a major sink for phosphorus in methanogenic coastal surface sediments. Geochem. Cosmochim. Acta 169, 217–235. https://doi.org/10.1016/j.gca.2015.09.012.

Ernstberger, H., Zhang, H., Tye, A., Young, S., Davison, W., 2005. Desorption kinetics of Cd, Zn, and Ni measured in soils by DGT. Environ. Sci. Technol. 39, 1591–1597. https://doi.org/10.1021/es048534d.

Gonzalez-Silva, B.M., Briones-Gallardo, R., Razo-Flores, E., Celis, L.B., 2009. Inhibition of sulfate reduction by iron, cadmium and sulfide in granular sludge. J. Hazard Mater. 172, 400–407. https://doi.org/10.1016/j.jhazmat.2009.07.022.

Ingall, E., Jahnke, R., 1997. Influence of water-column anoxia on the elemental fractionation of carbon and phosphorus during sediment diagenesis. Mar. Geol. 139, 219–229. https://doi.org/10.1016/s0025-3227(96)00112-0.

Jin, L., Lu, C.-Y., Ye, Y., Ye, G.-F., 2013. Soil respiration in a subtropical mangrove wetland in the Jiulong River estuary, China. Pedosphere 23, 678–685.

Kraal, P., Burton, E.D., Rose, A.L., Kocar, B.D., Lockhart, R.S., Grice, K., Bush, R.T., Tan, E., Webb, S.M., 2015. Sedimentary iron-phosphorus cycling under contrasting redox conditions in a eutrophic estuary. Chem. Geol. 392, 19–31. https://doi.org/10.1016/j.chemgeo.2014.11.006.

Laskov, C., Herzog, C., Lewandowski, J., Hupfer, M., 2007. Miniaturized photometrical methods for the rapid analysis of phosphate, ammonium, ferrous iron, and sulfate in pore water of freshwater sediments. Limnol Oceanogr. Methods 5, 63–71. https://doi.org/10.4319/lom.2007.5.63.

Lehtoranta, J., Ekholm, P., Pitkanen, H., 2009. Coastal eutrophication thresholds: a matter of sediment microbial processes. Ambio 38, 303–308. https://doi.org/10.1579/09-a-656.1.

Liao, E., Jiang, Y., Yan, X.-H., Chen, Z., Wang, J., Zhang, L., 2013. Allocation of marine environmental carrying capacity in the Xiamen Bay. Mar. Pollut. Bull. 75, 21–27. https://doi.org/10.1016/j.marpolbul.2013.08.023.

Lin, J., Sun, Q., Ding, S., Wang, D., Wang, Y., Chen, M., Shi, L., Fan, X., Tsang, D.C.W., 2017. Mobile phosphorus stratification in sediments by aluminum immobilization. Chemosphere 186, 644–651. https://doi.org/10.1016/j.chemosphere.2017.08.005.

Liu, Q., Ding, S., Chen, X., Sun, Q., Chen, M., Zhang, C., 2018. Effects of temperature on phosphorus mobilization in sediments in microcosm experiment and in the field. Appl. Geochem. 88, 158–166. https://doi.org/10.1016/j.apgeochem.2017.07.018.

Lovley, D.R., Phillips, E.J.P., 1988. Novel mode of microbial energy-metabolism - organic-carbon oxidation coupled to dissimilatory reduction of iron or manganese. Appl. Environ. Microbiol. 54, 1472–1480.

Markovic, S., Liang, A., Watson, S.B., Guo, J., Mugalingam, S., Arhonditsis, G., Morley, A., Dittrich, M., 2019. Biogeochemical mechanisms controlling phosphorus diagenesis and internal loading in a remediated hard water eutrophic embayment. Chem. Geol. 514, 122–137. https://doi.org/10.1016/j.chemgeo.2019.03.031.

Marz, C., Riedinger, N., Sena, C., Kasten, S., 2018. Phosphorus dynamics around the sulphate-methane transition in continental margin sediments: authigenic apatite and Fe(II) phosphates. Mar. Geol. 404, 84–96. https://doi.org/10.1016/j.margeo.2018.07.010.

Middelburg, J.J., Levin, L.A., 2009. Coastal hypoxia and sediment biogeochemistry. Biogeosciences 6, 1273–1293. https://doi.org/10.5194/bg-6-1273-2009.

Moses, C.O., Herman, J.S., 1991. Pyrite oxidation at circumneutral PH. Geochem. Cosmochim. Acta 55, 471–482. https://doi.org/10.1016/0016-7037(91)90005-p.

Muyzer, G., Stams, A.J.M., 2008. The ecology and biotechnology of sulphate-reducing bacteria. Nat. Rev. Microbiol. 6, 441–454. https://doi.org/10.1038/nrmicro1892.

Nriagu, J.O., 1972. Stability of vivianite and ion-pair formation in the system fe3(PO4)2-H3PO4H3PO4-H2o. Geochem. Cosmochim. Acta 36, 459–470. https://doi.org/10.1016/0016-7037(72)90035-X.

Pan, F., Guo, Z., Cai, Y., Liu, H., Wu, J., Fu, Y., Wang, B., Gao, A., 2019a. Kinetic exchange of remobilized phosphorus related to phosphorus-iron-sulfur biogeochemical coupling in coastal sediment. Water Resour. Res. https://doi.org/10.1029/2019wr025941.

Pan, F., Liu, H., Guo, Z., Cai, Y., Fu, Y., Wu, J., Wang, B., Gao, A., 2019b. Metal/metalloid and phosphorus characteristics in porewater associated with manganese geochemistry: a case study in the Jiulong River Estuary, China. In: Environmental Pollution (Barking, Essex: 1987), 255. https://doi.org/10.1016/j.envpol.2019.113134, 113134-113134.

Pan, F., Liu, H., Guo, Z., Li, Z., Wang, B., Cai, Y., Gao, A., 2019c. Effects of tide and season changes on the iron-sulfur-phosphorus biogeochemistry in sediment porewater of a mangrove coast. J. Hydrol. 568, 686–702. https://doi.org/10.1016/j.jhydrol.2018.11.002.

Pan, F., Liu, H., Guo, Z., Li, Z., Wang, B., Gao, A., 2017. Geochemical behavior of phosphorus and iron in porewater in a mangrove tidal flat and associated phosphorus input into the ocean. Cont. Shelf Res. 150, 65–75. https://doi.org/10.1016/j.csr.2017.09.012.

Paytan, A., McLaughlin, K., 2007. The oceanic phosphorus cycle. Chem. Rev. 107, 563–576. https://doi.org/10.1021/cr0503613.

Raven, M.R., Fike, D.A., Bradley, A.S., Gomes, M.L., Owens, J.D., Webb, S.A., 2019. Paired organic matter and pyrite delta S-34 records reveal mechanisms of carbon, sulfur, and iron cycle disruption during Ocean Anoxic Event 2. Earth Planet. Sci. Lett. 512, 27–38. https://doi.org/10.1016/j.epsl.2019.01.048.

Raven, M.R., Sessions, A.L., Adkins, J.F., Thunell, R.C., 2016. Rapid organic matter sulfurization in sinking particles from the Cariaco Basin water column. Geochem. Cosmochim. Acta 190, 175–190. https://doi.org/10.1016/j.gca.2016.06.030.

Roy, E.D., Nguyen, N.T., White, J.R., 2017. Changes in estuarine sediment phosphorus fractions during a large-scale Mississippi River diversion. Sci. Total Environ. 609, 1248–1257. https://doi.org/10.1016/j.scitotenv.2017.07.224.

Rozan, T.F., Taillefert, M., Trouwborst, R.E., Glazer, B.T., Ma, S.F., Herszage, J., Valdes, L.M., Price, K.S., Luther, G.W., 2002. Iron-sulfur-phosphorus cycling in the sediments of a shallow coastal bay: implications for sediment nutrient release and benthic macroalgal blooms. Limnol. Oceanogr. 47, 1346–1354. https://doi.org/10.4319/lo.2002.47.5.1346.

Slomp, C.P., VanderGaast, S.J., VanRaaphorst, W., 1996. Phosphorus binding by poorly crystalline iron oxides in North Sea sediments. Mar. Chem. 52, 55–73. https://doi.org/10.1016/0304-4203(95)00078-x.

Teasdale, P.R., Batley, G.E., Apte, S.C., Webster, I.T., 1995. Pore-water sampling with sediment peepers. Trac. Trends Anal. Chem. 14, 250–256. https://doi.org/10.1016/0165-9936(95)91617-2.

Thibault, P.-J., Rancourt, D.G., Evans, R.J., Dutrizac, J.E., 2009. Mineralogical confirmation of a near-P:Fe=1:2 limiting stoichiometric ratio in colloidal P-bearing ferrihydrite-like hydrous ferric oxide. Geochem. Cosmochim. Acta 73, 364–376. https://doi.org/10.1016/j.gca.2008.10.031.

Tyrrell, T., 1999. The relative influences of nitrogen and phosphorus on oceanic primary production. Nature 400, 525–531. https://doi.org/10.1038/22941.

van Bodegom, P.M., Stams, A.J.M., 1999. Effects of alternative electron acceptors and temperature on methanogenesis in rice paddy soils. Chemosphere 39, 167–182.

Wang, D., Gong, M., Li, Y., Xu, L., Wang, Y., Jing, R., Ding, S., Zhang, C., 2016. In situ,

high-resolution profiles of labile metals in sediments of lake Taihu. Int. J. Environ. Res. Public Health 13. https://doi.org/10.3390/ijerph13090884.
Widerlund, A., Davison, W., 2007. Size and density distribution of sulfide-producing microniches in lake sediments. Environ. Sci. Technol. 41, 8044–8049. https://doi.org/10.1021/es071510x.
Xiong, Y., Guilbaud, R., Peacock, C.L., Cox, R.P., Canfield, D.E., Krom, M.D., Poulton, S.W., 2019. Phosphorus cycling in Lake Cadagno, Switzerland: a low sulfate euxinic ocean analogue. Geochem. Cosmochim. Acta 251, 116–135. https://doi.org/10.1016/j.gca.2019.02.011.
Xu, D., Wu, W., Ding, S., Sun, Q., Zhang, C., 2012. A high-resolution dialysis technique for rapid determination of dissolved reactive phosphate and ferrous iron in pore water of sediments. Sci. Total Environ. 421, 245–252. https://doi.org/10.1016/j.scitotenv.2012.01.062.
Yang, C., Li, Y., Zhou, Y., Zheng, W., Tian, Y., Zheng, T., 2012. Bacterial community dynamics during a bloom caused by Akashiwo sanguinea in the Xiamen sea area, China. Harmful Algae 20, 132–141. https://doi.org/10.1016/j.hal.2012.09.002.
Yin, H., Wang, J., Zhang, R., Tang, W., 2019. Performance of physical and chemical methods in the co-reduction of internal phosphorus and nitrogen loading from the sediment of a black odorous river. Sci. Total Environ. 663, 68–77. https://doi.org/10.1016/j.scitotenv.2019.01.326.
Zhang, H., Davison, W., Miller, S., Tych, W., 1995. In-situ high-resolution measurements of fluxes of NI, CU, FE, and MN and concentrations of ZN and CD in porewaters by DGT. Geochem. Cosmochim. Acta 59, 4181–4192. https://doi.org/10.1016/0016-7037(95)00293-9.